

Wearable Stretchable Dry and Self-Adhesive Strain Sensors with Conformal Contact to Skin for High-Quality Motion Monitoring

Shan Wang, Yuanlai Fang, Hao He, Lei Zhang, Chang'an Li, and Jianyong Ouyang*

Wearable stretchable strain sensors can have important applications in many areas. However, the high noise is a big hurdle for their application to monitor body movement. The noise is mainly due to the motion artifacts related to the poor contact between the sensors and skin. Here, wearable stretchable dry and self-adhesive strain sensors that can always form conformal contact to skin even during body movement are demonstrated. They are prepared via solution coating and consist of two layers, a dry adhesive layer made of bio-compatible elastomeric waterborne polyurethane and a sensing layer made of a non-adhesive composite of reduced graphene oxide and carbon nanotubes. The adhesive layer makes the sensors conformal to skin, while the sensing layer exhibits a resistance sensitive to strain. The sensors are used to accurately monitor both small- and large-scale body movements, including various joint movements and muscle movements. They can always generate high-quality signals even on curvilinear skin surface and during irregular skin deformation. The sensitivity is remarkably higher while the noise is significantly lower than the non-adhesive strain sensors. They can also be used to monitor the movements along two perpendicular directions, which cannot be achieved by the non-adhesive strain sensors.

1. Introduction

Wearable stretchable strain sensors have attracted tremendous attention because they can be used to continuously monitor human health situation at low cost.^[1] Their operation mechanism is usually the sensitivity of their resistance or capacitance to strain.^[2] Because of their high mechanical stretchability, they can be used to monitor skin deformation caused by muscle movement or joint movements.^[3] Strain sensors in literature are usually not adhesive to skin, and they are mounted on skin


surface along one direction with non-stretchable adhesive tape or bandage at the two ends. Although they can overall follow the muscle movement or skin deformation because of their mechanical stretchability, their contact to skin is not conformal. Because the skin deformation is not 1D and usually irregular, the strain generated in the strain sensors can deviate from the actual skin deformation, particularly when the strain direction is different from the longitudinal direction of the sensors or skin surface is irregular. Hence, they cannot accurately perceive the skin deformation during body movement. This gives rise to severe motion artifacts.^[4] In the even worse case, some body movements may cause the slippage or delamination of the sensors from skin, and fault signals are thus detected. Motion artifacts and fault signal are big problems for the practical application of strain sensors.^[5] These problem becomes more severe for the strain sensors to monitor joint move-

ment that can generate large strain. Monitoring the joint movement is important for healthcare, particularly for ageing people and patients with injuries or Parkinson's disease or motion control disorder.^[6] The joint motion problems can be caused by many factors such as ageing, joint diseases like osteoarthritis, rheumatoid arthritis, gout, and bursitis, accident trauma like fracture and scoliosis, even excessive exercise and long-time bad postures.^[7]

The motion artifacts and fault signals mainly arise from the contact between strain sensor and skin. The contact can be greatly improved by making the strain sensors adhesive to skin. Both dry and wet adhesives are used to improve the contact. The dry adhesives include ultrathin films and biomimetic structure. Although ultrathin films can be adhesive to human skin, they are difficult to manufacture and handle.^[8] Their contact to skin cannot be uniform as well. Biomimetic structures like Gecko- or octopus-inspired micro/nano-structures can be adhesive to skin. Thus, micro/nano-structures like microneedles, microfibers, and nanopillars were used as the adhesive layer of strain sensors.^[9] They can enhance the sensitivity and lower the noise. Nevertheless, the micro/nano-structures require complex fabrication processes like photolithography and etching. They can also make the users uncomfortable for long term use. Besides the dry adhesive approaches, **adhesive hydrogels using**

S. Wang, Y. Fang, H. He, Dr. L. Zhang, C. Li, Prof. J. Ouyang
Department of Materials Science and Engineering
National University of Singapore
Singapore 117574, Singapore
E-mail: mseoj@nus.edu.sg

S. Wang
State Key Lab of Silicon Materials
School of Materials Science and Engineering
Zhejiang University
Hangzhou 310027, China

 The ORCID identification number(s) for the author(s) of this article can be found under <https://doi.org/10.1002/adfm.202007495>.

DOI: 10.1002/adfm.202007495

catechol and its derivatives are also investigated.^[1a,10] Although they can have high sensitivity, water evaporation during use can affect the contact and thus generate noise and even fault signals. The hydrogel residual on the skin is also another concern. In addition, the adhesive hydrogel can be sticky to clothes on body during use. It is of significance to develop wearable dry strain sensors that are adhesive and thus form conformal contact to skin even during body movement.

In this work, wearable strain sensors with an adhesive elastomer layer are fabricated through facile solution processing. Because they can always form conformal contact with the skin even during body movement, they can always generate high-quality signals. The sensitivity is remarkably higher and the noise is saliently lower than non-adhesive strain sensors. The advantages become more remarkable for curvilinear skin and irregular change in the skin surface. They can be used to monitor a movement along two different directions simultaneously.

2. Results and Discussion

2.1. Adhesive Layer of the Strain Sensors

The dry-adhesive strain sensors are consisted of a sensing layer and an adhesive layer as shown in **Figure 1a**. Two types of anionic water-dispersible polyurethanes (WPUs) with different properties are used in the two layers. Both of them are biocompatible elastomers consisted of hard and soft segments.^[11] The polymer matrix for the top sensing layer is non-adhesive WPU (nWPU) supplied by the Taiwan PU Corporation (WPU-372D). The nWPU composites of conductive reduced graphene oxide (rGO) and multi-walled carbon nanotubes (CNTs) are used for the top sensing layer. This sensing layer has high mechanical stretchability and a resistance sensitive to the strain. But it is not adhesive since both the polymer matrix and the nanofillers are not adhesive. As shown in **Figure 1b**, the adhesive WPU (aWPU) is composed of polyurethane backbone and hydrophilic internal emulsifier (2,2-bis(hydroxymethyl)propionic acid, DMPA). It can be dispersed in water due to the carboxylate ion. Its properties strongly depend on the ratio of the hard segment (HS) to the soft segment (SS). More SS can make it softer and more adhesive, while more HS can give rise to higher elasticity while less adhesiveness.^[11b,12]

Several aWPUs with different HS to SS ratios were synthesized in order to find the optimal HS-to-SS ratio for their application as the adhesive layer. As displayed in **Figure 1c**, the HS is prepared by the copolymerization of isophorone diisocyanate, DMPA and ethylene glycol, and the SS is polyethylene glycol with an average molecular weight of 2000. The detailed synthesis procedure is provided in **Figure S1**, Supporting Information. The aWPUs with the HS mass percentages of 25, 30, 35, and 40 wt% were prepared, and they are denoted as aWPU-25%, aWPU-30%, aWPU-35%, and aWPU-40% in this paper. The HS and SS of WPUs can form the hard and soft domains (**Figure 1d**). The hard domain formation is related to the hydrogen bonding between urethane and urea groups and the high glass transition temperature (T_g) of 55–78 °C of

HS, and the soft domains are formed by SS with a low T_g of –69 to –40 °C.^[13a,b]

All the aWPUs can be dispersed well in water, and the appearance of the aWPU emulsions are related to the HS percentage (**Figure 1e**). Higher the HS percentage, whiter in color and less transparent of the aWPU emulsion. This can be attributed to the larger gel particles at higher HS percentage as evidenced by the dynamic light scattering (DLS) results (**Figure 1f**). The average particle sizes of aWPU-25%, aWPU-30%, aWPU-35%, and aWPU-40% are 39, 52, 154, and 204 nm, respectively. The WPU gel particles have a structure of the core made of aggregated hydrophobic segments and surrounded by an outside layer with the ionic groups.^[11a,12] Therefore, a higher HS percentage can give rise to longer hydrophobic segments in the core and thus increase gel particle size.

Free-standing aWPU films with different HS percentages were prepared by drop casting the aWPU emulsions on polytetrafluoroethylene substrate and then peeling off. Their mechanical properties were studied by the tensile experiments (**Figure 2a**). The tensile strength and the Young's modulus decrease with the increasing HS percentage. High plastic deformation can be observed particularly for aWPU-25% because the aWPUs are soft and tough elastomers.^[13c]

Figure 2b displays the dependences of the Young's modulus and elongation at break on the HS percentage of aWPU films. Among them, the aWPU-25% film exhibits the highest elongation at break of 3000% and the lowest Young's modulus of 295 kPa. As the HS percentage increases, the Young's modulus and tensile strength increase while the elongation at break decreases. This can be attributed to the much stronger intermolecular interactions of HS than SS.^[11b,14] This is consistent with that reported in literatures.^[11b]

The lap shear strengths of aWPU samples were measured by placing an aWPU film between two glass slides (**Figure 2c**). The lap shear results are related to the sample resistance to flow under shear and depend on both the cohesive and adhesive strengths of the adhesives.^[15] It can provide information on the adhesiveness of the sample to the substrate. **Figure 2d** shows the load versus the displacement curves of the aWPU-25%, aWPU-30%, aWPU-35%, and aWPU-40% films. There are three stages. At the first stage, the force increases with the displacement and then reaches a peak. The second stage appears after the peak force. The cracks initiate and propagate in the bonded region of the adhesive and the substrate, leading to the decrease in force. At the last stage, the joint between the adhesive and substrates fails, and a plateau appears in the curve. The lap shear strength depends on the HS percentage of the aWPUs. At the HS percentages of 30%, 35%, and 40%, the cohesion inside the aWPU films is higher than the adhesion to substrate.^[11c,13a,15a] As shown in **Figure 2e**, the lap shear strengths of aWPU-30%, aWPU-35%, and aWPU-40% are 130, 87, and 34 kPa, respectively, and they correspond to the adhesive failure. This can be attributed to the mechanical flexibility of the aWPUs. Higher mechanical flexibility gives rise to higher lap shear strength. However, abnormal results were observed when the HS content was lowered to 25%. The lap shear strength of aWPU-25% is only 44 kPa, remarkably lower than that of aWPU-30%. This can be attributed to the cohesive failure because of the low cohesion inside aWPU-25%

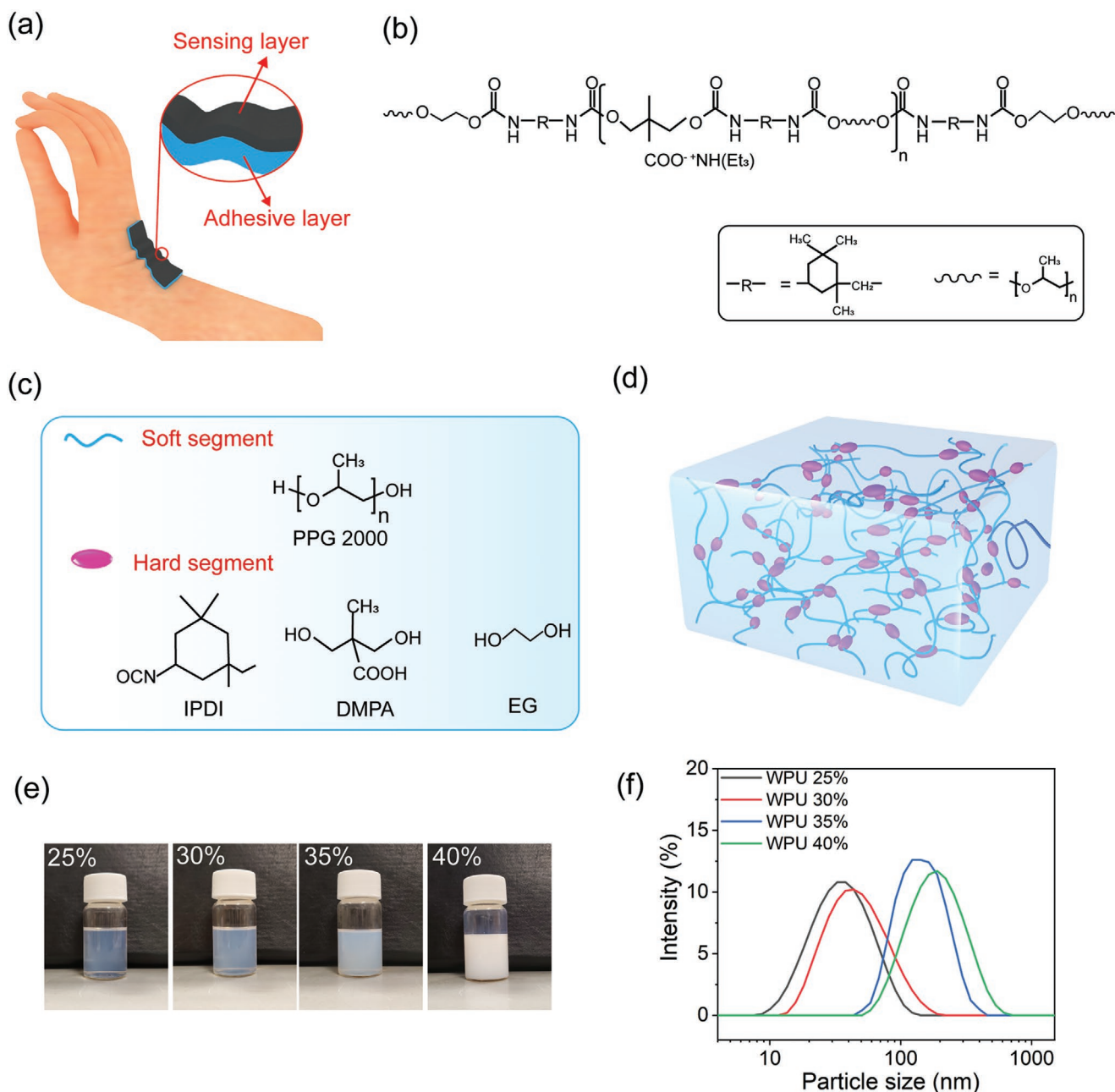


Figure 1. a) Schematic structure of a strain sensor with a top sensing layer and a bottom adhesive layer. b) Chemical structure of aWPU. c) Hard segment (HS) and soft segment (SS) of aWPU. d) Schematic illustration of the microstructure of aWPU with hard and soft domains formed by HS and SS, respectively. e) Photographs of aWPU-25%, aWPU-30%, aWPU-35%, and aWPU-40% dispersions. f) Dynamic light scattering study on the particle size distributions of aWPU-25%, aWPU-30%, aWPU-35%, and aWPU-40% dispersions.

(Figure 2f). Because the aWPU-30% film has the highest lap shear strength, it can be the best option as the adhesive layer of the strain sensors.

As mentioned above, an aWPU with high mechanical flexibility can have higher adhesiveness. The adhesion mechanism can be attributed to the two types of interactions between aWPU and substrate. One is the physical adsorption due to intermolecular interactions between aWPU and substrate, including primary bonds such as covalent through isocyanate (–NCO) or polar groups (–NH, C=O)

to the surface or secondary van der Waals forces especially hydrogen bonds. Apart from the functional groups of aWPU, the intermolecular interaction depends on the contact area between aWPU and the adherend. A soft adhesive can have large contact area with the adherend and thus high intermolecular interactions per unit area. Another factor is the mechanical interlocking with irregular and rough surface of the adherend. A softer adhesive can easily penetrate into the surface of the adherend and form interlocks, which also increase the adhesiveness.^[16]

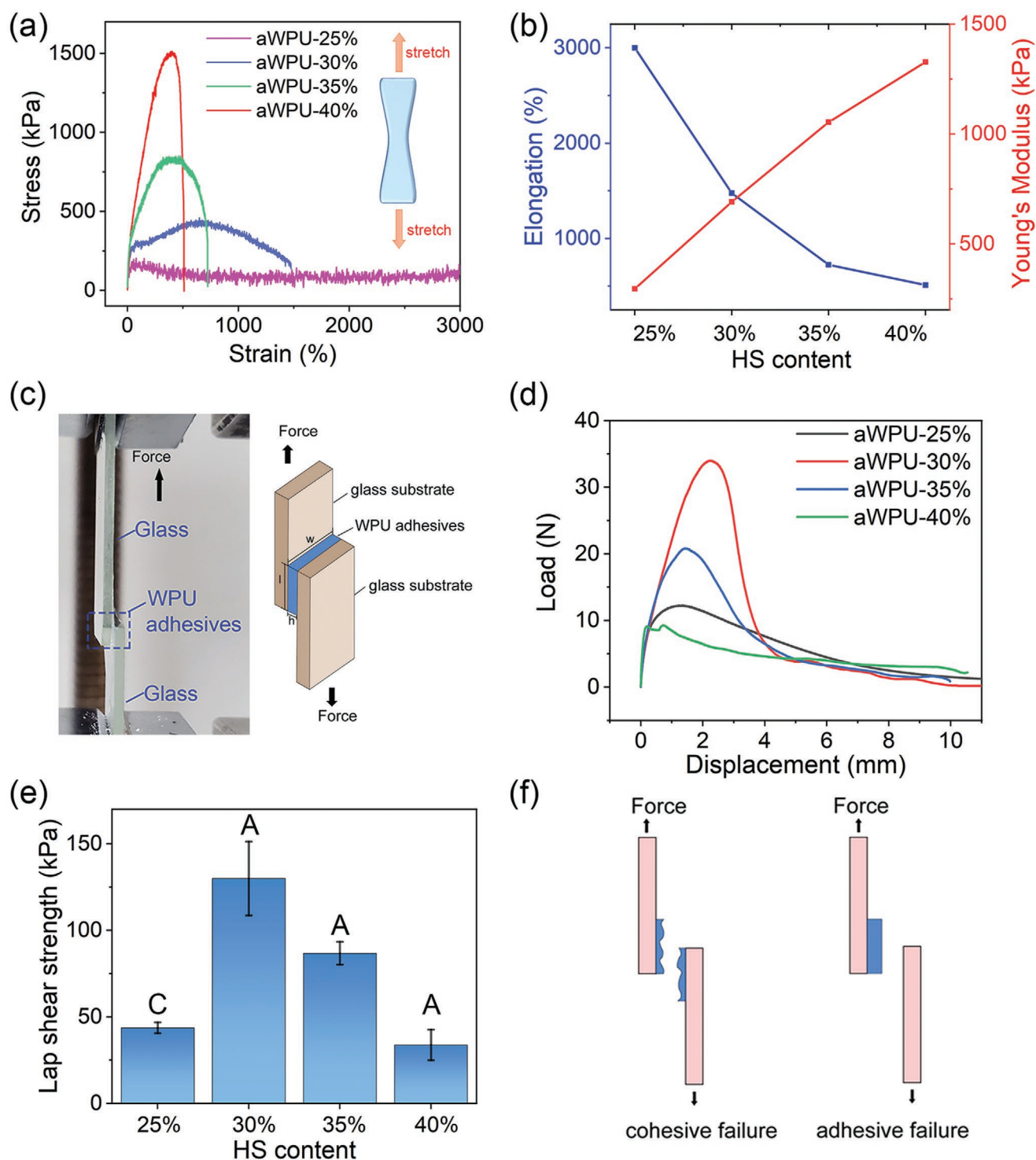


Figure 2. a) Stress–strain curves of free-standing aWPU-25%, aWPU-30%, aWPU-35%, and aWPU-40% films. b) Dependences of the Young's modulus and elongation at break on the HS content of aWPU films. c) Photo and schematic illustration of the setup for the lap shear testing. d) Load versus displacement curves for aWPU-25%, aWPU-30%, aWPU-35%, and aWPU-40%. e) Lap shear strength of the aWPU films with different HS contents. C and A represent the cohesive failure and adhesive failure, respectively. f) Schematic illustrations for the cohesive and adhesive failures of adhesives.

2.2. Sensing Layer of the Strain Sensors

The sensing layer is a composite of nWPU-rGO/CNTs. As shown in Figure 3a, the sensing layer is prepared by drop casting, and

the aWPU adhesive layer is then coated on the sensing layer. The gel particle size of the dispersions of nWPU, rGO, and CNTs were studied by DLS (Figure 3b,c). The average particle sizes of nWPU and CNTs dispersions are 231 and 162 nm,

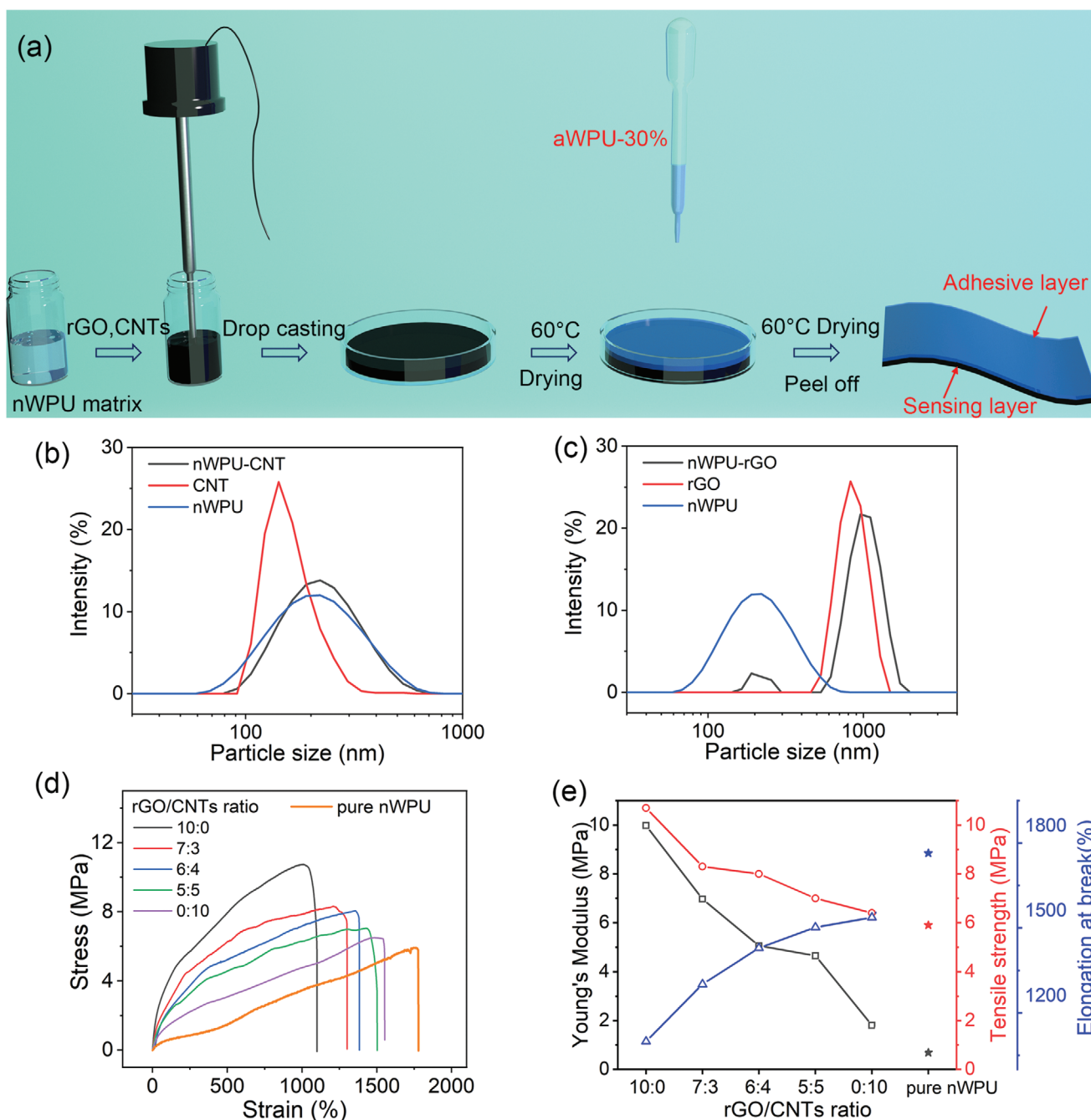


Figure 3. a) Schematic fabrication of the adhesive strain sensors. DLS study on the particle size distributions of b) nWPU, CNT, and nWPU-CNT and c) nWPU, rGO, and nWPU-rGO aqueous dispersions. d) Stress–strain curves of nWPU-rGO/CNTs composite films with different rGO/CNTs mass ratios and a neat nWPU film. The total filler concentration was 4 wt% for all the composites. e) Dependences of the Young’s modulus, tensile strength, and elongation at break of nWPU-rGO/CNTs composites on the rGO/CNTs mass ratio of the fillers and neat nWPU. The total filler concentration was 4 wt% for all the composites.

respectively. The nWPU-CNTs dispersion has an average particle size of 230 nm, and its size distribution is slightly narrower than the nWPU dispersion. There are two peaks at 995 and 220 nm, respectively, for the nWPU-rGO dispersion. By comparison with the results of nWPU and rGO dispersions, the two peaks can be ascribed to the size distributions of rGO and nWPU, respectively, in water. The average size of rGO particles in the

dispersion of nWPU-rGO is larger than that of the neat rGO dispersion. The increase in the rGO particle size suggests that some nWPU chains may surround rGO sheets. All the dispersions are homogeneous and quite stable. No precipitation was observed after 48 h (Figure S2, Supporting Information).

A strain sensor should be flexible enough to follow the skin deformation, and its flexibility is related to its thickness.

Because both nWPU and aWPU are elastomers, their films with a thickness of hundred micrometers or less can have high mechanical flexibility. Therefore, composite films of nWPU-rGO/CNTs with a thickness of about 100 μm were prepared by drop casting, and they were used for the measurement of mechanical properties. The total filler concentration is 4 wt% for all the composites. As shown in Figure 3d,e, all the composites are highly stretchable, and the mechanical properties of the composites depend on the rGO-to-CNT ratio. The nWPU-rGO composite has the smallest elongation at break of 1100%, and the nWPU-CNTs composite has the highest elongation at break of 1537%. Both the Young's modulus and the tensile strength decrease while the elongation at break increases with the decreasing rGO-to-CNT ratio. Presumably, this is related to the interfacial interaction between nWPU and the nanofillers. Because rGO has a high specific surface area than CNTs and some functional groups like hydroxyl, epoxide, and carboxyl groups, its reinforcement effect is stronger than CNTs.^[3c,17]

2.3. Adhesive Strain Sensors

The devices with the sensing and adhesive layers can be used as conformal wearable strain sensors. The insulating adhesive

layer prevents the body from electrical stimulus, and the non-adhesive sensing layer makes the sensor surface not sticky. The adhesive layer can bind well with the sensing layer. No delamination between them occurs after repeated mounting/demounting and repeated stretching/releasing on substrates including human skins and glass slides. The peel strengths of the strain sensors to a porcine skin were studied by the 180° peel testing (Figure 4a). The peel strength is the average load per unit width of the bonding line required to separate the bonded materials where the angle of separation is 180°. Figure 4b shows the peel force versus the displacement curves of the strain sensors with different aWPUs. The peel force increases first and turns to a plateau after reaching a maximum value. The peel force at the plateau is the peel strength of the adhesive. The peel strength decreases with the increasing HS percentage of aWPUs (Figure 4c). Although aWPU-25% exhibits the highest peel strength, it corresponds to the cohesive failure. Residual could be observed on the substrate surface after peeling off as shown in the inset of Figure 4c. No residual was observed for the sensors with other aWPUs including aWPU-30%, aWPU-35%, and aWPU-40%. Their peeling off is related to the adhesive failure. The peel strengths to the porcine skin are 36, 28, and 13 N m^{-1} for the sensors with aWPU-30%,

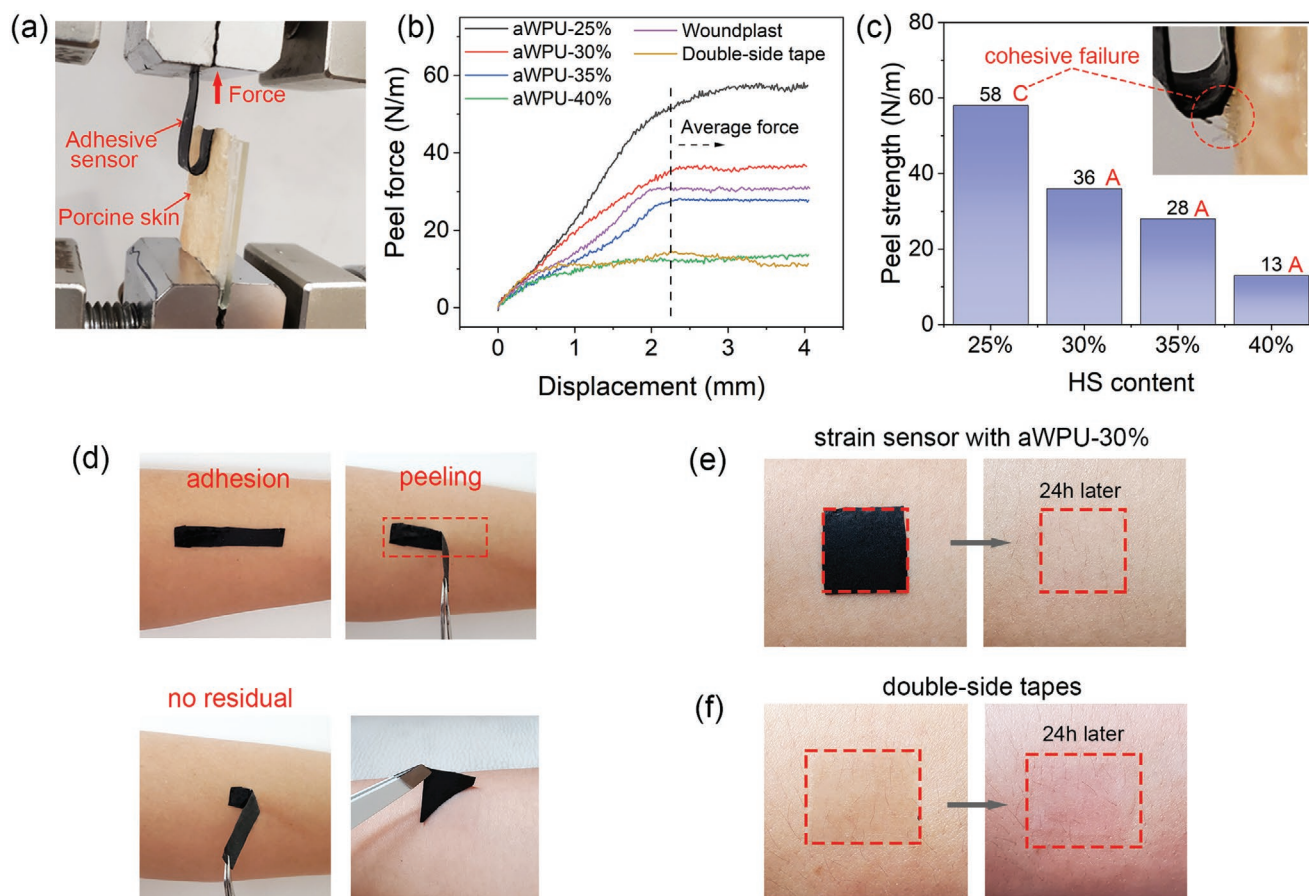


Figure 4. a) Photo of the setup for the 180° peel testing. b) Peel force versus displacement curves of the strain sensors with aWPU of 25%, 30%, 35%, and 40% HS on a porcine skin. c) The peel strengths of the strain sensors with aWPU of 25%, 30%, 35%, and 40% HS. d) Demonstration of the adhesion between a strain sensor and human skin. The adhesive layer was aWPU-30%. No residual was left on skin after the sensor was peeled off. e) Photos of a strain sensor with the adhesive layer of aWPU-30% on skin and then peeled off after 24 h. f) Photos of a 3M double-side tape on skin and then peeled off after 24 h.

aWPU-35%, and aWPU-40%, respectively. The peel strengths of aWPU strain sensors to glass substrate were also measured, showing similar relationship between the peel strengths and the HS percentage of aWPU (Figure S3, Supporting Information). Because aWPU-30% has a high peel strength and leaves no residual after peeling off, it is used for the adhesive layer of the strain sensors.

The strain sensors with aWPU-30% can be easily attached to human skin and peeled off. As shown in Figure 4d, a strain sensor with aWPU-30% was mounted to the forearm of a person. It is compliant to the skin and keeps intimate contact with the skin even during arm movements. No slippage or delamination could be observed. After the sensor was peeled off, no residual was left.

The adhesive layer of the strain sensors has excellent biocompatibility because polyurethane is a popular biomaterial. A sensor with aWPU-30% was mounted on the skin for 24 h and then peeled off. It did not cause irritation of the skin, and the volunteer did not feel pain during peeling off. Almost nothing could be observed on the skin after peeling off (Figure 4e). Control experiments were also conducted using a 3M double-side tape. The 3M double-side tape could cause skin irritation, and the volunteer felt painful when it was peeled off (Figure 4f). Red spots could be observed on the skin after use for 24 h.

The resistance of the strain sensors is sensitive to strain. The gauge factor (GF) is determined by the change in the resistance caused by a strain, $GF = (\Delta R/R_0)/\varepsilon$ with $\Delta R = |R - R_0|$ and R_0 and R being the original resistance and the resistance at the applied strain of ε . Generally, to sense minor strains caused by subtle motions such as face, throat or pulses requires high GF and high signal-to-noise, while monitoring large strains needs broad sensing range. To sense both the small and large strains, the sensors should have high GF and broad sensing range. A sensor with high GF and wide sensing range can be used to monitoring body movements of minor or large strain.

In order to have high GF and wide sensing range, both CNTs and rGO are used as the nanofillers in the sensing layer. If there are only CNTs in the composite, the resistance variation by strain is small because CNTs are usually entangled together. It is difficult to break down the connection of all CNTs.^[18] On the other hand, if only rGO is used, the separation among the rGO sheets is very sensitive to the strain, and it can saliently affect the charge tunneling across the rGO sheets. As a result, the sensors can have a high GF but a small sensing range.^[3c] At an appropriate nanofiller loading and ratio of CNTs to rGO, their co-existence can give rise to both high GF and wide sensing range.

The total weight percentage of the nanofillers in all strain sensors is 4 wt% in the sensing composite layer. Figure 5b presents the resistance responses of an aWPU-rGO/CNTs (6:4) sensor when the strain is increased step by step. The resistance at a strain of 120% is nearly 50% of the original value. The curve of $\Delta R/R_0$ versus ε is almost linear in the strain range of 0–60% or 60–120% (Figure 5c). The GF values in these two ranges are $GF_1 = 7.2$ and $GF_2 = 89$, respectively.

The rGO/CNTs ratio affects not only the mechanical properties of the nWPU-rGO/CNTs films but also the strain sensitivity of the sensors (Figure 5d). Strain sensors with higher rGO/CNTs ratios show higher resistance variation at the same

strain. Figure 5e summarizes the GFs and sensing ranges of five devices with different rGO/CNTs ratios. The nWPU-rGO/CNTs (10:0) sensors have the highest GF_1 of 281 while the lowest sensing range of 23%. The nWPU-rGO/CNTs (10:0) sensors have the most broad sensing range of 240% while the lowest GF_1 of 1.96. The strain sensors based on nWPU-rGO/CNTs (6:4) can have a high GF_1 of 7.2 and GF_2 of 89 as well as a broad sensing range of 120%. Therefore, they are used to monitor human motions.

2.4. Application of the Dry-Adhesive Strain Sensors in Motion Monitoring

Wearable strain sensors are often mounted on skin to monitor the body movement, particularly the movement of joints, because the movements of the joints such as the neck, shoulder, wrist, spine, and ankle can be affected by ageing, injury, and diseases.^[5a,6a,19] Hence, monitoring these joint motions is essential for healthcare and patient rehabilitation.

Figure 6 presents the signals from an adhesive strain sensor mounted on an index finger of a volunteer. A smooth curve with well-defined peaks and dips was recorded during the finger movement. In contrast, the peak value randomly varies and salient noise can be observed when a non-adhesive sensor is used. The high signal quality generated by the adhesive strain sensor can be attributed to its conformal contact to skin. This can significantly lower the motion artifacts. The skin surface changes from flat to convex when the finger bends. When the adhesive strain sensors were used to monitor the convex knee movement, the signal quality is also much higher than the non-adhesive strain sensors (Figure S4, Supporting Information).

As modeled in Figure 7a, some joints can move along two opposite directions. The skin surface can change to convex along one direction while concave along the opposite direction. For example, the wrist can bend up or bend down. When a sensor is mounted to the back side of a wrist, the skin surface changes to concave and convex when the wrist bends up and down, respectively (Figure 7b). Negative angle is defined when the wrist bends up, and the angle is positive when the wrist bends down. As shown in Figure 7c, when an adhesive strain sensor is used, signals can be detected when the wrist bends up or down, and the resistance variation is consistent with the bending degree. However, signals can be detected only when the wrist bends down, that is, the skin surface changes to convex, when a non-adhesive strain sensor is used (Figure 7d). No signal can be observed when the wrist bends up, that is, at a negative bending degree. This is caused by the delamination of the non-adhesive strain sensor from the skin when the skin surface becomes concave. Instead, the adhesive strain sensor does not delaminate from the skin surface regardless of flat, convex, or concave skin surface. In addition, the adhesive strain sensor exhibits higher sensitivity than the non-adhesive one. At the bending degree of 45°, the $\Delta R/R_0$ values are about 22% and 11% for the adhesive and non-adhesive strain sensors, respectively. The sensitivity of the former is about twice of the latter.

Figure 7e,f show the signals of monitoring the continuous wrist bending by attaching an adhesive or non-adhesive strain sensor to the back of the wrist. Smooth curves are always

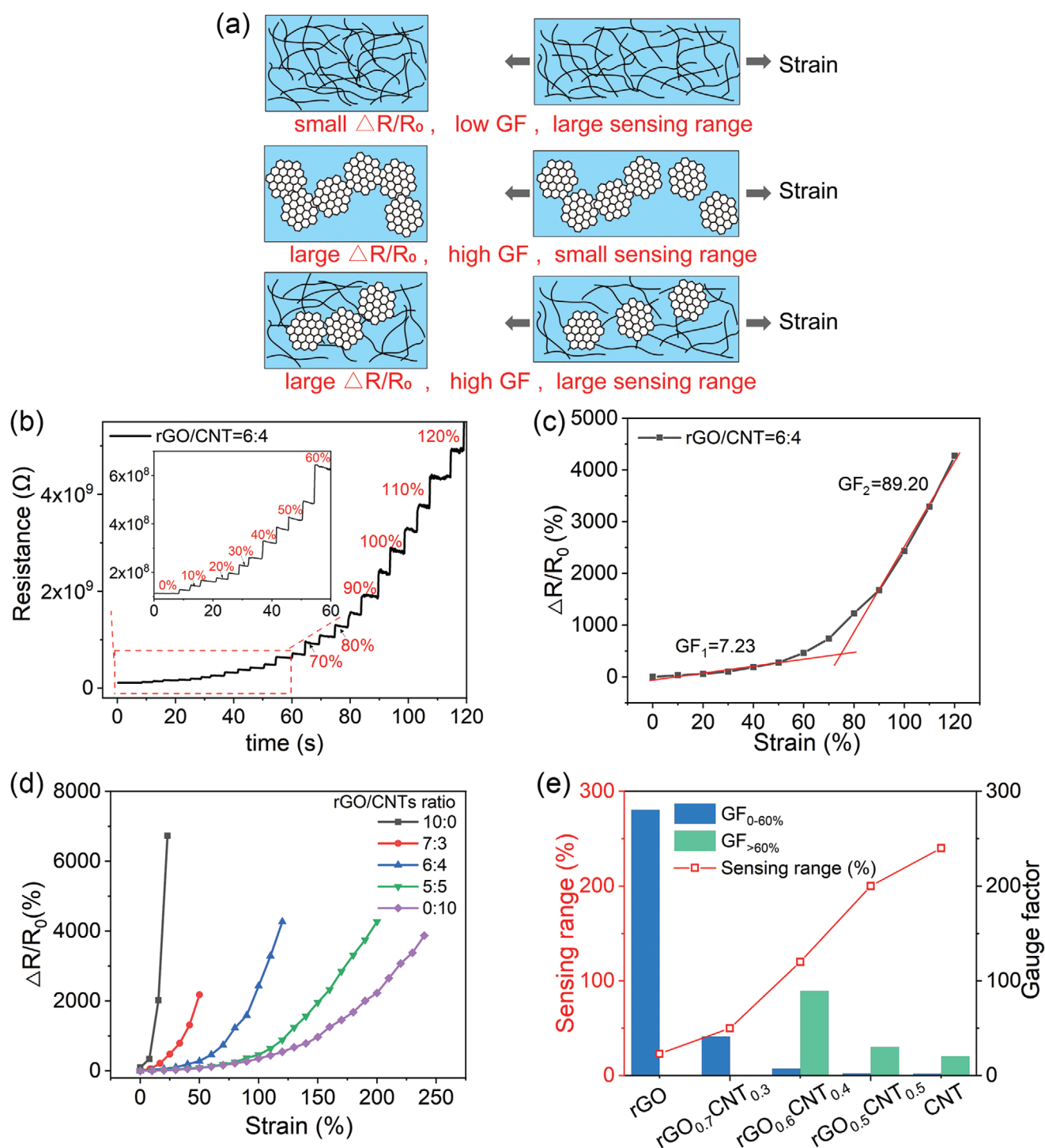


Figure 5. a) Schematic illustration of the conductive networks in the polymer composites of CNTs, rGOs and rGO/CNTs at rest and under strain. b) Resistance responses of a strain sensor with nWPU-rGO/CNTs(6:4) when different strains are applied step by step. c) Variation of $\Delta R/R_0$ of a nWPU-rGO/CNTs(6:4) sensor with the strain. d) Variations of the resistance of the strain sensors with different rGO/CNTs ratios with the strain. e) GF_1 , GF_2 and sensing ranges of strain sensors with different rGO/CNTs ratios.

obtained for the adhesive strain sensors. In comparison, the non-adhesive strain sensor exhibits signals with lower intensity and much higher noise when the wrist bends down, and only noise is obtained when the wrist bends up.

As shown in **Figure 8**, similar differences of adhesive strain sensors from the non-adhesive strain sensors can be observed when they are used to monitor the movements of neck and ankle, which can bend along two opposite directions as well.

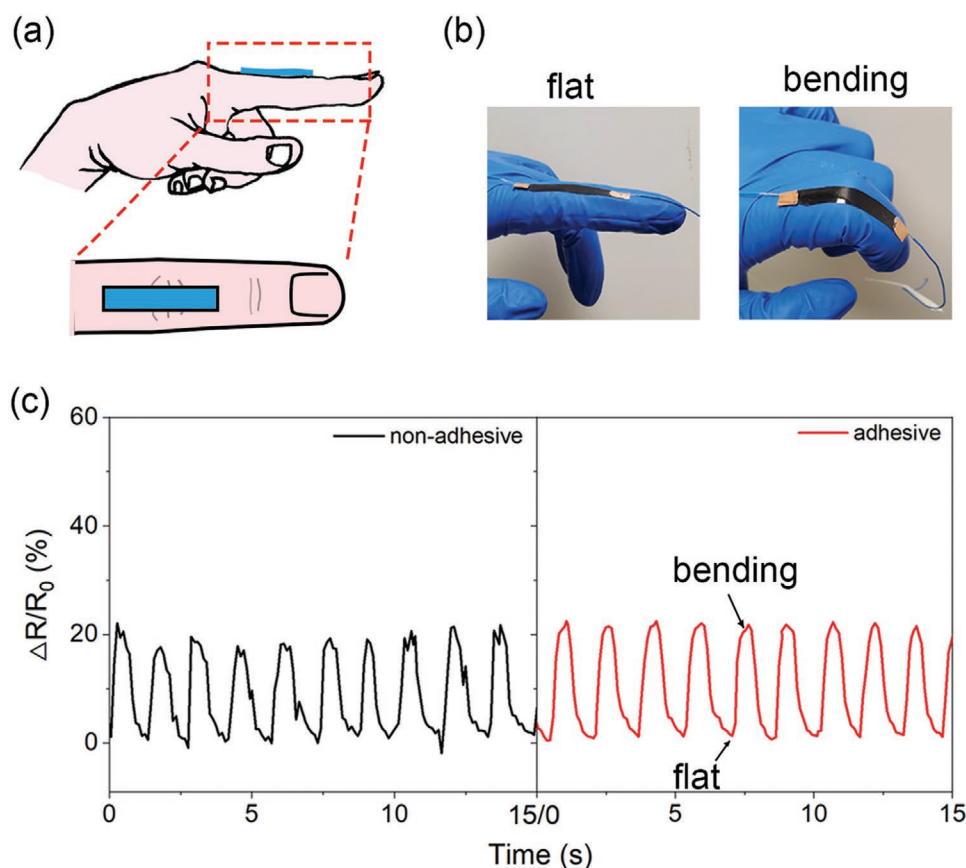


Figure 6. a) Schematic illustration of a strain sensor on an index finger. b) Photos of strain sensor on the index finger. c) Signals from non-adhesive and adhesive sensors when the finger bent down.

The adhesive strain sensors can always exhibit signals with much higher quality than the non-adhesive ones. When attached to the inner side of an elbow to monitor the concave elbow bending, the adhesive strain sensor shows higher intensity and lower noise than the non-adhesive strain sensor (Figure S5, Supporting Information).

It is very often that a skin may have irregular surface and the surface irregularly changes during joint movements. For example, the larynx skin is usually curvilinear and irregularly changes during swallowing (Figure 9a). To monitor the swallowing activity can provide important information for oropharyngeal dysphagia, which is a control disorder phenomenon and can be induced by diseases like Parkinson's disease, stroke, dementia, and ageing related problems.^[1e,20] Oropharyngeal dysphagia can lead to dehydration, malnutrition, or even death without proper treatment. When a strain sensor is attached to the larynx skin, its resistance increases when the thyroid notch moves up during swallowing and reaches the maximum at the uppermost stage (Figure 9a,b). The resistance then decreases when the thyroid notch moves down. The adhesive strain sensor can always form an intimate contact with the curvilinear larynx skin, while only part of the non-adhesive sensor can contact with the larynx skin. As a result, the peak $\Delta R/R_0$ value is around 76% for the adhesive strain sensor when the volunteer swallows the saliva. This signal intensity is greater than six times of that (around 12%) of the non-adhesive sensor.^[21]

The larynx movement is related to the volume of food or beverage to swallow. An adhesive strain sensor was used to monitoring the swallowing of 10, 15, and 20 mL waters (Figure 9c). The signal intensity increased with the increasing water volume. The signal intensity at the same water volume is always much higher than that using the non-adhesive strain sensor (Figure 9d).

The adhesive strain sensors are particularly important when the skin surface changes to concave, because the non-adhesive strain sensors can partially or fully delaminated from the convex skin surface. The strain sensors were used to monitor this kind of skin deformation caused by the muscle movements, including the calf muscle and vastus medialis muscle movements (Figure S6, Supporting Information). The adhesive strain sensors can exhibit high-quality signals, while the signals are very noisy for the non-adhesive ones. When a strain sensor is placed on skin, its longitudinal direction can deviate from the strain direction of the skin deformation (Figure S7, Supporting Information). If the sensor is not adhesive, the strain in the sensor cannot be uniform, and noise can be thus generated. The signal can be greatly improved when an adhesive strain sensor is used.

Because all the parts of the adhesive strain sensors can keep conformal contact to skin, they can be used to monitor the muscle movements along two different directions. The muscle movement or skin deformation during body

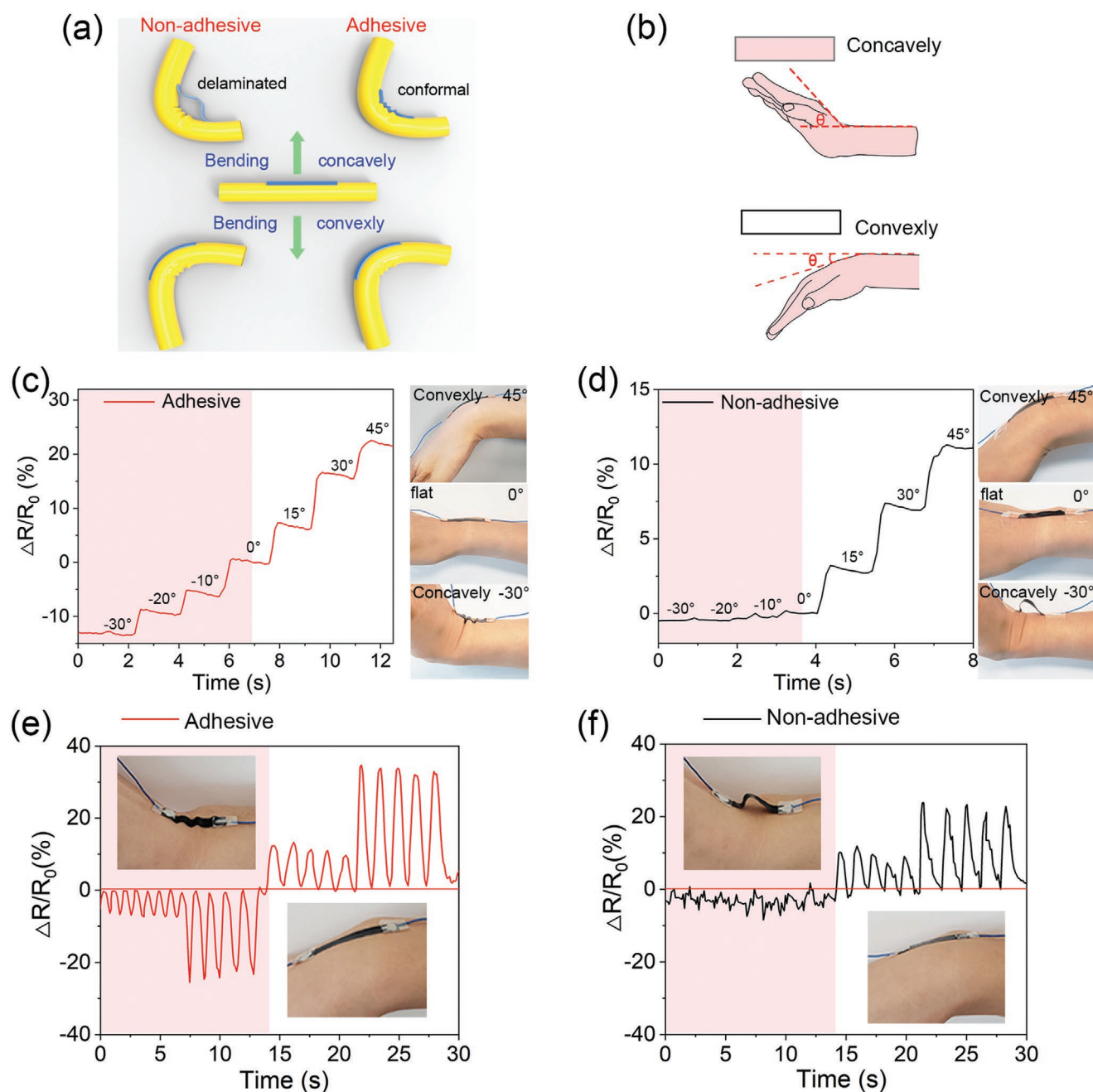


Figure 7. a) Schematic illustration for monitoring the joint bendings concavely and convexly with adhesive and non-adhesive strain sensors. b) Concave and convex skin surfaces when the wrist bends up and down, respectively. Resistance responses of the c) dry-adhesive and d) non-adhesive strain sensors at different bending angles of the wrist. The negative bending angles correspond to bending up with concave skin surface, and positive angles correspond to bending down with convex skin surface. Monitoring continuous wrist bending with e) a dry-adhesive strain sensor and f) a non-adhesive strain sensor.

movement is not 1D. But they are usually monitored along only one direction. If a non-adhesive strain sensor is used for the 2D detection, tapes must be used at four different sides, and the signal can be twisted. **Figure 10** presents monitoring the wrist bending by an adhesive strain sensor along two perpendicular directions. The skin deformation is mainly along the y -axis, and thus high signal intensity is observed. Apart from the y -axis, remarkable signals are detected along the x -axis as well.

It is worth to point out that the aWPU layer may not increase the noise related to the hysteresis. As shown in Figure S8, Supporting Information, hysteresis can be observed on the loading and unloading stress–strain curves of both nWPU and aWPU-30%, and aWPU-30% has more remarkable hysteresis than nWPU. However, aWPU-30% has a much lower Young's modulus than nWPU. Because of the good adhesion of aWPU-30% to both nWPU and skin, a thin layer of aWPU-30% should not affect the strain of the sensing layer during the skin deformation.

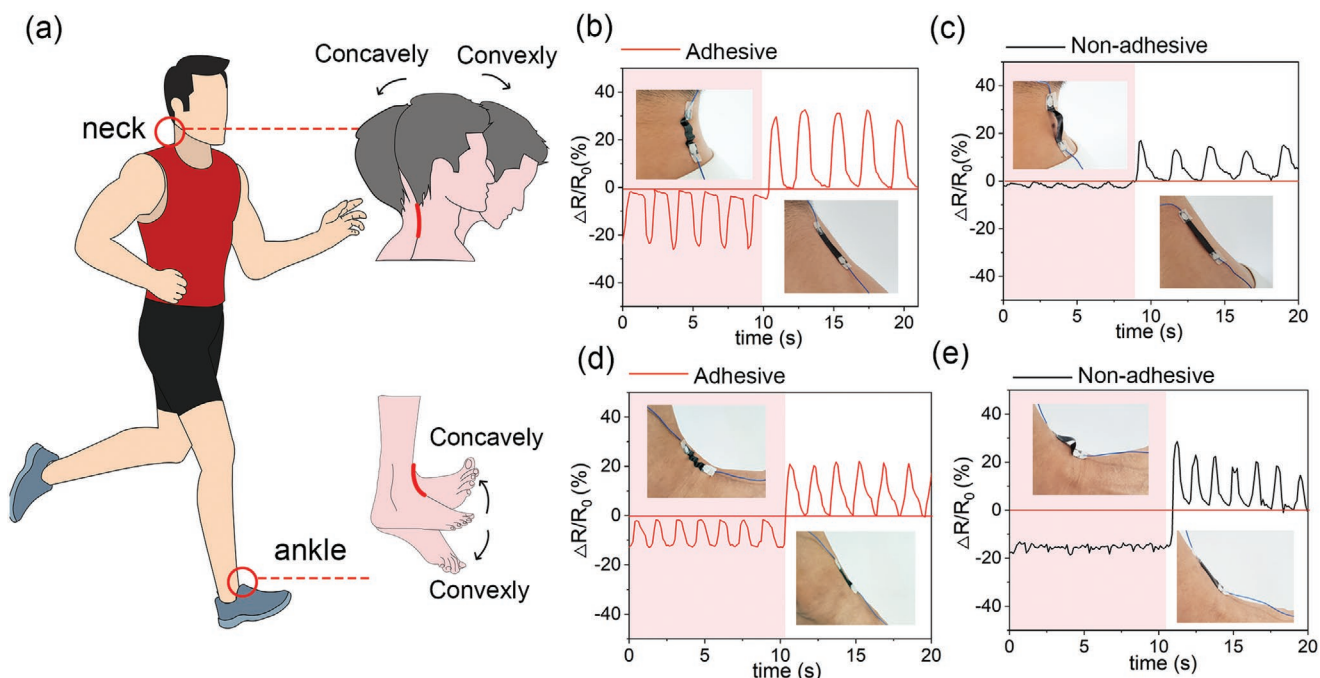


Figure 8. a) Schematic illustration of strain sensors on neck and ankle during movements. Signals for the neck movements monitored with b) an adhesive strain sensor and c) a non-adhesive strain sensor. Monitoring the ankle movements with d) an adhesive strain sensor and e) a non-adhesive strain sensor.

3. Conclusions

In this work, a dry and self-adhesive strain sensor composed of a sensing layer and an adhesive layer was prepared by solution

processing. Both layers are stretchable. The sensing layer is made of non-adhesive WPU composites of rGO and CNTs. It can have high gauge factor and wide sensing range. Adhesive WPU is coated on the sensing layer for conformal contact of

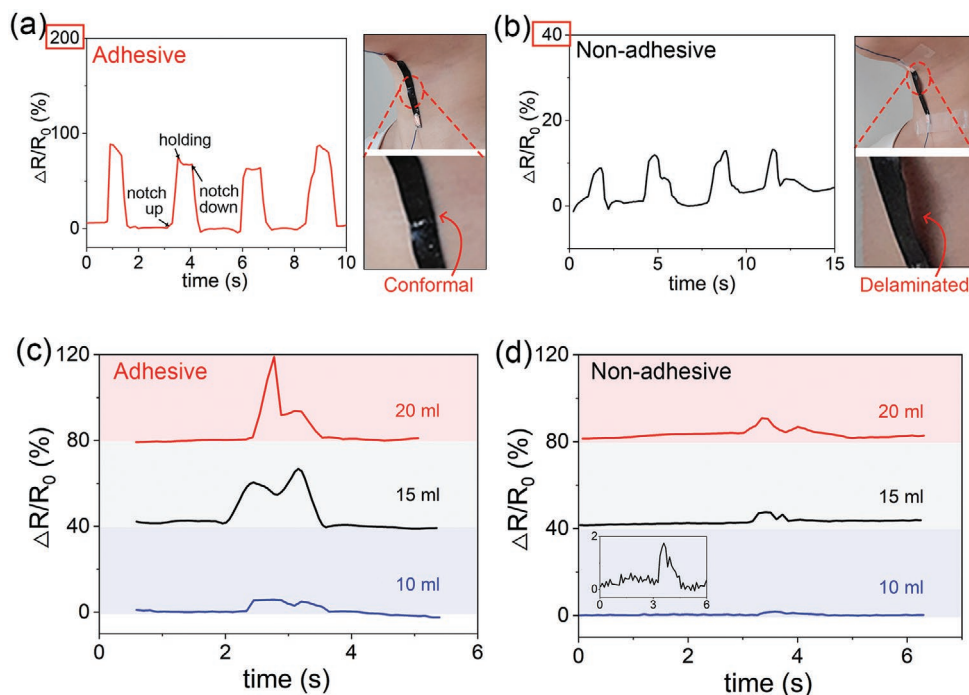


Figure 9. Resistance responses of a) the dry-adhesive and b) non-adhesive strain sensors during salvia swallowing. $\Delta R/R_0$ of the c) dry-adhesive and d) non-adhesive strain sensors during swallowing 10, 15, and 20 mL water.

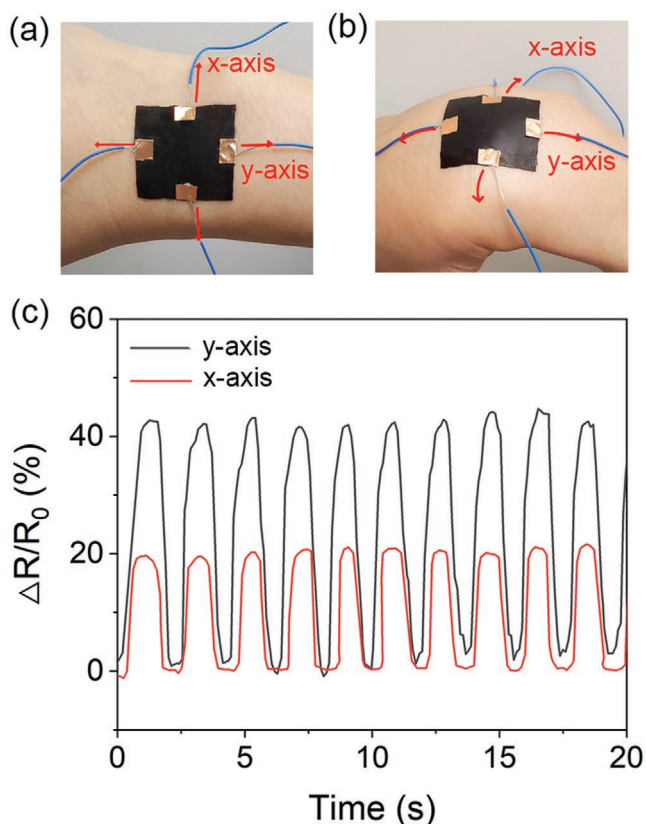


Figure 10. Photos of a dry-adhesive strain sensor on the wrist a) before bending and b) during bending. c) Resistances responses of the dry-adhesive strain sensor in the longitudinal (*y*-axis) and transverse (*x*-axis) directions when the wrist bends down.

the sensors to skin. The adhesive strain sensors are used to monitor body movements with large or small strains, including the movements of finger, wrist, knee, ankle, and muscles. High quality signal with low noise is always observed. The signal quality is much higher than the control non-adhesive strain sensors. Their advantages become more significantly when they are used on curvilinear skin surface or irregular skin deformation. The adhesiveness also enables them to monitor the movements along two perpendicular directions and high-quality signals can be detected along both directions.

Supporting Information

Supporting Information is available from the Wiley Online Library or from the author.

Acknowledgements

This work was financially supported by a grant from the Ministry of Education, Singapore (R-284-000-220-114). Shan Wang is grateful to the China Scholarships Council for the oversea scholarship (No. 201906320194). All relevant ethical regulations were complied with and informed consent was obtained from all participants. The study protocol was approved by the NUS Institutional Review Board (NUS-IRB REFERENCE CODE: S-20-019).

Conflict of Interest

The authors declare no conflict of interest.

Keywords

adhesive, motion artifacts, strain sensor, stretchable, wearable electronics

Received: September 2, 2020

Revised: October 8, 2020

Published online:

- [1] a) B. Ryplida, K. D. Lee, I. In, S. Y. Park, *Adv. Funct. Mater.* **2019**, *29*, 1903209; b) S. Wang, K. F. Chen, M. Wang, H. S. Li, G. R. Chen, J. Liu, L. H. Xu, Y. Jian, C. D. Meng, X. Y. Zheng, *J. Mater. Chem. C* **2018**, *6*, 4737; c) S. Chen, Y. j. Song, D. Ding, Z. Ling, F. Xu, *Adv. Funct. Mater.* **2018**, *28*, 1802547; d) B. C. K. Tee, J. Ouyang, *Adv. Mater.* **2018**, *30*, 1802560; e) M. K. Kim, C. Kantarcigil, B. Kim, R. K. Baruah, S. Maity, Y. Park, K. Kim, S. Lee, J. B. Malandraki, S. Avlani, A. Smith, S. Sen, M. A. Alam, G. Malandraki, C. H. Lee, *Sci. Adv.* **2019**, *5*, eaay3210; f) J. C. Yang, J. Mun, S. Y. Kwon, S. Park, Z. Bao, S. Park, *Adv. Mater.* **2019**, *31*, 1904765.
- [2] a) J. H. Pu, X. J. Zha, M. Zhao, S. Li, R. Y. Bao, Z. Y. Liu, B. H. Xie, M. B. Yang, Z. Guo, W. Yang, *Nanoscale* **2018**, *10*, 2191; b) L. Zhang, K. Chen, S. Wang, S. Chen, S. Niu, Z. Wang, P. Du, *Mater. Lett.* **2018**, *233*, 306.
- [3] a) Q. Trung Tran, N.-E. Lee, *Adv. Mater.* **2016**, *28*, 4338; b) J. Park, M. Kim, Y. Lee, H. S. Lee, H. Ko, *Sci. Adv.* **2015**, *1*, e1500661; c) S. Wang, G. Chen, S. Niu, K. Chen, T. Gan, Z. Wang, H. Wang, P. Du, C. W. Leung, S. Qu, *ACS Appl. Mater. Interfaces* **2019**, *11*, 48331; d) Z. Tang, D. Yao, D. Du, J. Ouyang, *J. Mater. Chem. C* **2020**, *8*, 2741.
- [4] a) G. Shi, Z. Zhao, J.-H. Pai, I. Lee, L. Zhang, C. Stevenson, K. Ishara, R. Zhang, H. Zhu, J. Ma, *Adv. Funct. Mater.* **2016**, *26*, 7614; b) W. Li, J. Guo, D. Fan, *Adv. Mater. Technol.* **2017**, *2*, 1700070; c) X. Shi, S. Liu, Y. Sun, J. Liang, Y. Chen, *Adv. Funct. Mater.* **2018**, *28*, 1800850; d) D. Du, Z. Tang, J. Ouyang, *J. Mater. Chem. C* **2017**, *6*, 883; e) R. Zhou, P. Li, Z. Fan, D. Du, J. Ouyang, *J. Mater. Chem. C* **2017**, *5*, 1544.
- [5] a) Y. Lu, Z. Liu, H. Yan, Q. Peng, R. Wang, M. E. Barkey, J.-W. Jeon, E. K. Wujcik, *ACS Appl. Mater. Interfaces* **2019**, *11*, 20453; b) H. Liu, H. Xiang, Y. Wang, Z. Li, L. Qian, P. Li, Y. Ma, H. Zhou, W. Huang, *ACS Appl. Mater. Interfaces* **2019**, *11*, 40613.
- [6] a) M. Amit, L. Chukoskie, A. J. Skalsky, H. Garudadri, T. N. Ng, *Adv. Funct. Mater.* **2020**, *30*, 1905241; b) M. M. Rodgers, G. Alon, V. M. Pai, R. S. Conroy, *J. Rehabil. Assistive Technol. Eng.* **2019**, *6*, 1.
- [7] a) E. M. Badley, A. Tennant, *Ann. Rheum. Dis.* **1992**, *51*, 366; b) J. Cushnaghan, P. Dieppe, *Ann. Rheum. Dis.* **1991**, *50*, 8.
- [8] a) S. Liu, R. Zheng, S. Chen, Y. Wu, H. Liu, P. Wang, Z. Deng, L. Liu, *J. Mater. Chem. C* **2018**, *6*, 4183; b) J. W. Jeong, W. H. Yeo, A. Akhtar, J. J. Norton, Y. J. Kwack, S. Li, S. Y. Jung, Y. Su, W. Lee, J. Xia, H. Cheng, Y. Huang, W. S. Choi, T. Bretl, J. A. Rogers, *Adv. Mater.* **2013**, *25*, 6839; c) X. Huang, Y. Liu, H. Cheng, W.-J. Shin, J. A. Fan, Z. Liu, C.-J. Lu, G.-W. Kong, K. Chen, D. Patnaik, S.-H. Lee, S. Hage-Ali, Y. Huang, J. A. Rogers, *Adv. Funct. Mater.* **2014**, *24*, 3846.
- [9] a) D.-M. Drotlef, M. Amjadi, M. Yunusa, M. Sitti, *Adv. Mater.* **2017**, *29*, 1701353; b) C. Pang, J. H. Koo, A. Nguyen, J. M. Caves, M. G. Kim, A. Chortos, K. Kim, P. J. Wang, J. B. Tok, Z. Bao, *Adv. Mater.* **2015**, *27*, 634; c) S. Baik, H. J. Lee, D. W. Kim, J. W. Kim, Y. Lee, C. Pang, *Adv. Mater.* **2019**, *31*, 1803309.

- [10] a) C. Cui, C. Shao, L. Meng, J. Yang, *ACS Appl. Mater. Interfaces* **2019**, *11*, 39228; b) Z. Song, W. Li, Y. Bao, F. Han, L. Gao, J. Xu, Y. Ma, D. Han, L. Niu, *ACS Appl. Mater. Interfaces* **2018**, *10*, 42826.
- [11] a) J. Y. Jang, Y. Kuk Jhon, I. W. Cheong, J. H. Kim, *Colloids Surf., A* **2002**, *196*, 135; b) R. Li, J. A. Ton Loontjens, Z. Shan, *Eur. Polym. J.* **2019**, *112*, 423; c) H. Honarkar, *J. Dispersion Sci. Technol.* **2018**, *39*, 507; d) E. J. Shin, S. M. Choi, *Adv. Exp. Med. Biol.* **2018**, *1077*, 251.
- [12] M. A. Pérez-Limiñana, F. Arán-Aís, A. M. Torró-Palau, A. C. Orgilés-Barceló, J. M. Martín-Martínez, *Int. J. Adhes. Adhes.* **2005**, *25*, 507.
- [13] a) X. Liu, K. Xu, H. Liu, H. Cai, J. Su, Z. Fu, Y. Guo, M. Chen, *Prog. Org. Coat.* **2011**, *72*, 612; b) Z. Gao, J. Peng, T. Zhong, J. Sun, X. Wang, C. Yue, *Carbohydr. Polym.* **2012**, *87*, 2068. c) D. R. Roberts, S. J. Holder, *J. Mater. Chem.* **2011**, *21*, 8256.
- [14] P. Florian, K. K. Jena, S. Allauddin, R. Narayan, K. V. S. N. Raju, *Ind. Eng. Chem. Res.* **2010**, *49*, 4517.
- [15] a) B. D. B. Tiu, P. Delparastan, M. R. Ney, M. Gerst, P. B. Messersmith, *ACS Appl. Mater. Interfaces* **2019**, *11*, 28296; b) A. H. Hofman, I. A. van Hees, J. Yang, M. Kamperman, *Adv. Mater.* **2018**, *30*, 1704640; c) X. Liu, Q. Zhang, Z. Gao, R. Hou, G. Gao, *ACS Appl. Mater. Interfaces* **2017**, *9*, 17645.
- [16] a) S. Ebnesajjad, A. H. Landrock, in *Adhesives Technology Handbook*, 3rd ed., (Eds: S. Ebnesajjad, A. H. Landrock), William Andrew Publishing, Boston **2015**, p. 1; b) B. T. Michal, E. J. Spencer, S. J. Rowan, *ACS Appl. Mater. Interfaces* **2016**, *8*, 11041.
- [17] a) L. Ci, J. Suhr, V. Pushparaj, X. Zhang, P. M. Ajayan, *Nano Lett.* **2008**, *8*, 2762; b) P. Li, D. Du, L. Guo, Y. Guo, J. Ouyang, *J. Mater. Chem. C* **2016**, *4*, 6525.
- [18] K. Ke, P. Potschke, N. Wiegand, B. Krause, B. Voit, *ACS Appl. Mater. Interfaces* **2016**, *8*, 14190.
- [19] S. Park, S. Ahn, J. Sun, D. Bhatia, D. Choi, K. S. Yang, J. Bae, J.-J. Park, *Adv. Funct. Mater.* **2019**, *29*, 1808369.
- [20] a) C. A. Jones, E. L. Meisner, C. K. Broadfoot, S. P. Rosen, C. R. Samuelsen, T. M. McCulloch, *Front. Appl. Math. Stat.* **2018**, *4*, 23; b) Y. Lee, B. Nicholls, D. Sup Lee, Y. Chen, Y. Chun, C. Siang Ang, W.-H. Yeo, *Sci. Rep.* **2017**, *7*, 46697.
- [21] C. Pang, J. H. Koo, A. Nguyen, J. M. Caves, M. G. Kim, A. Chortos, K. Kim, P. J. Wang, J. B. Tok, Z. Bao, *Adv. Mater.* **2015**, *27*, 634.